Three-dimensional magnetic field reconstruction in the VKS experiment through Galerkin transforms

To cite this article: J Boisson and B Dubrulle 2011 *New J. Phys.* **13** 023037

View the article online for updates and enhancements.

Three-dimensional magnetic field reconstruction in the VKS experiment through Galerkin transforms

J Boisson[1] **and B Dubrulle**

SPEC/IRAMIS/CEA Saclay, and CNRS (URA 2464), 91191 Gif-sur-Yvette Cedex, France
E-mail: jean.boisson@cea.fr

Abstract. We present a method for three-dimensional (3D) magnetic field reconstruction based on Galerkin transforms. We test it over synthetic fields and real solenoidal (velocity) fields, measured in a water experiment. Our study shows that reliable reconstructions are possible provided that the probes are sufficiently sampled and located in shifted configurations. A preliminary application of our method is performed on results obtained in the VKS dynamo experiment (Bourgoin *et al* 2002 *Phys. Fluids* **14** 3046). We show that the stationary dynamos obtained with counter-rotating impellers are mainly axisymmetric, with a non-axisymmetric part that decreases with increasing Reynolds numbers. Most of the azimuthal energy is localized near the (iron) impellers, confirming their importance in the dynamo process.

[1] Author to whom any correspondence should be addressed.

Contents

1. Introduction

The magnetic field is an essential ingredient of most natural objects, and numerous campaigns of observations or experiments are devoted to its measurement or modeling. A problem often encountered in this process is the sparsity of measurements: only a limited number of measurements, at a limited number of positions, are usually available. Specific techniques must then be implemented with the data to reconstruct the magnetic field outside the measurement points, so as to get information about their geometry, intensity, direction, etc. Classic examples are reconstruction of the terrestrial or solar magnetic field. In the first case, data are rather numerous at the surface of the earth and reconstruction is achieved by fitting a set of basis functions, usually spherical harmonics or spherical caps, to magnetic data. In the case of the sun, data are sparser, and the reconstruction can usually only be achieved through physical assumptions. For example, Solanki *et al* [1] use magnetic data issued from vector spectropolarimetry of the He I 1083 nm multiplet, formed near the coronal base, and assume that the He line is formed along tubes of magnetic flux as the active region emerges through the chromosphere into the corona. The He line emission then forms in coronal-like loops. With this assumption, a three-dimensional (3D) magnetic field can be constructed that can be compared with extrapolations from deeper layers. Similar problems can be found in laboratory experiments. For example, electromagnetic velocity probes usually require measurement of the distribution of the 3D magnetic field in the whole measuring volume out of the probe. Clever
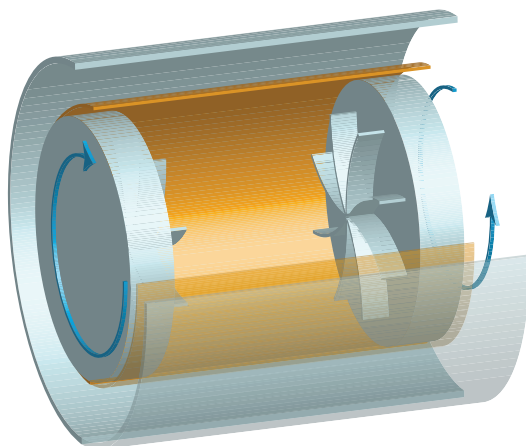
Figure 1. (a) Sketch of the VKS experiment geometry, including the probe locations. The z-axis of the cylindrical coordinates is taken as the x-axis of the experiment, i.e. the axial extension of the cylinder. The gap in between the inner and the outer cylinder is filled with sodium at rest. The inner container radius R is taken as the length scale.

assumptions about exciting currents and numerical solution of a Laplace equation allow for reconstruction of the 3D magnetic field from a mere measurement of the distribution of the normal component of the magnetic field on the surface of the probe [2]. In this paper, we focus on the case of the von Karman sodium (VKS) experiment, a laboratory facility designed for studying the turbulent fluid dynamo effect, i.e. the spontaneous generation of a magnetic field from turbulent motion of liquid sodium. In that experiment, the magnetic field measurements are localized only along a few magnetic sensors, thereby avoiding large disturbances of the measurements onto the flow of liquid sodium. The reconstruction of the full 3D magnetic field from these sparse measurements therefore implies technical processing of the magnetic data. Here, we describe a solution inspired by geophysical methods, involving fitting a set of suitable Galerkin basis functions to magnetic data.

2. Method

2.1. Geometry

The setup corresponding to the VKS experiment is sketched in figure 1 [13]. A cylindrical vessel has a fixed aspect ratio of $h/R = 1.8$, where $R(h)$ denotes the radius (height) of the vessel that is filled with liquid sodium. We consider a cylindrical coordinate system (r, φ, z) such that the axial vessel extension lies along z. Choosing R as the length scale, and introducing $L = h/2R = 0.9$, the variation ranges of the dimensionless cylindrical polar coordinates (r, φ, z) inside the experimental vessel are therefore $(0 \leqslant r \leqslant 1, -\pi \leqslant \varphi \leqslant +\pi, -L \leqslant z \leqslant +L)$. Our magnetic field reconstruction, however, also extends beyond the vessel boundaries, i.e. for $r > 1$, thanks to suitable boundary conditions (see below).

The fluid is stirred by two independent rotating so-called TM73 impellers [15, 16]. The impellers are fitted with curved blades, and can be rotated independently at frequencies F_1 and F_2.

Magnetic measurements are carried out using 3D Hall probes, and recorded with a National Instruments PXI digitizer. Both a single-point (three components) probe (hereafter labeled G-probe) and custom-made arrays of 10 (three components) probes (hereafter called SM-array) are used. The array is made of Sentron 2SA-1M Hall sensors located every 28 mm along a line. The different possible locations of the probes are sketched in figure 1.

2.2. Brief overview

A given VKS experiment provides us with a set of measurements of the (three components of the) magnetic field at N different sparse locations. To reconstruct the magnetic field in the whole space, we expand it on a set of well-chosen (see below) Galerkin functions $\mathbf{G}_i$,

$$\mathbf{B}(r, \varphi, z) = \sum_{i=1}^{M} b_i \mathbf{G}_i(r, \varphi, z), \tag{1}$$

where M is the number of modes of the reconstruction. Then, by imposing that the expansion matches the three components of the measured fields at the N measurement points, we obtain a set of $3N$ equations with M unknown (the coefficients of the expansion b_i). Inverting the systems thus provides the values of b_i and thus the reconstruction at that resolution. Of course, one cannot hope to reconstruct the field with a resolution larger than the number of measurements (i.e. $M < 3N$ to obtain good results). In addition, the possible non-uniqueness of the solution suggests the use of $M \ll 3N$ in order to allow for robustness of the inversion through redundancy. Since N is typically of the order of 1–10 (41 at most), this means that only a small number of Galerkin modes will be allowed in the reconstruction procedure. To obtain meaningful results, it is therefore mandatory to choose an optimal Galerkin basis, such that a small number of modes capture the large-scale structure of the experimental fields. This means that the Galerkin basis satisfies both the solenoidal condition and the boundary conditions of the magnetic field. We therefore now describe how to implement these constraints on the choice of the basis, following the recent works [3, 4].

2.3. Boundary conditions

Through the cylindrical coordinate system, the system is naturally periodic in the φ-direction. Boundary conditions must, however, be specified in the vertical and radial directions.

2.3.1. Vertical boundaries $z = \pm L$. As in pseudo-spectral simulations [15], the inversion procedure can be greatly simplified if one considers a 'periodized' version of the problem, in which the magnetic field is assumed periodic in the axial direction. It is, however, not possible to use the unit cell as the interval $z \in [-L; L]$ because the magnetic field is not naturally periodic over this cell. To avoid discontinuities and Gibbs phenomena (artifact oscillations of the reconstructed magnetic field near the discontinuity), we have thus chosen to use as a unit cell the whole range $z \in [-L; 3L]$, which is twice the original physical domain. Doing so yields magnetic field components that are continuous everywhere.

2.3.2. Radial boundary $r = 1$. The boundary conditions at $r = 1$ are set by the condition that both the magnetic field components and the derivative $\partial_r B_r$ are continuous at $r = 1$—the last condition stems from the solenoidal nature of B-, i.e. they match continuously the exterior

domain solution. Note that many numerical methods to deal with the $r = 1$ boundary conditions have been developed, based e.g. on boundary element formalism [24], on integral equation [26] or on spectral finite elements [25]. Here, we choose simple ways to manage these boundary conditions, compatible with our Galerkin decomposition. In the following, we consider three main possibilities:

- External insulating. If the medium surrounding the fluid is insulating, we obtain the following condition for the exterior solution,

$$\nabla \times \mathbf{B} = \mathbf{0}, \quad \nabla \cdot \mathbf{B} = \mathbf{0}, \quad \Rightarrow \Delta \mathbf{B} = \mathbf{0}. \tag{2}$$

  In the case of the spatially homogeneous magnetic permeability we are considering, the magnetic field must also be continuous and finite over all space, and vanish for $r \to \infty$.

- Ferromagnetic ($\mu_r = \infty$) wall at $r = 1$. In that case, we assume that the field is zero at $r > 1$, and that $B_z = B_\phi = 0$ at $r = 1$. This case mimics the situation where the fluid is surrounded by a ferromagnetic wall.

- The general case. In that case, we do not specify the boundary conditions at $r = 1$ for B_r and B_ϕ.

2.4. Galerkin basis

2.4.1. General case. Following [3, 4], we first switch from the usual cylindrical components $\mathbf{B} = (B_r, B_\varphi, B_z)$ to the new components $\mathbf{B} = (B_+, B_-, B_z)$ such that $B_\pm = (B_r \pm \mathrm{i}B_\varphi)/2$. Due to the periodic conditions in φ and z, it is natural to introduce the general decomposition over eigenmodes of the Helmoltz operator as

$$\mathbf{B} = \begin{pmatrix} B_+ \\ B_- \\ B_z \end{pmatrix} = \sum_{n=1}^{N} \sum_{m=-M}^{M} \sum_{k=-P\pi/2L}^{P\pi/2L} \begin{pmatrix} C_+^{nmk} J_{m+1}(\mu_{nmk}r) \\ C_-^{nmk} J_{m-1}(\mu_{nmk}r) \\ C_z^{nmk} J_m(\mu_{nmk}r) \end{pmatrix} \exp(\mathrm{i}m\varphi + \mathrm{i}kz), \tag{3}$$

with $C_{\pm,z}^{nmk} = (C_{\pm,z}^{n-m-k})^*$ to enforce the reality of the field and the numbers μ_{nmk} have to be chosen so as to respect boundary conditions. The coefficients $C_{\pm,z}^{nmk}$ are the spectral coefficients of our decomposition and are uniquely associated with our initial field $\mathbf{B}$. We then write symbolically the value of $\mathbf{B}$ in the Galerkin space as GT($\mathbf{B}$) (for Galerkin transform) with

$$\mathrm{GT}(\mathbf{B}) = \begin{pmatrix} C_+^{nmk} \\ C_-^{nmk} \\ C_z^{nmk} \end{pmatrix}. \tag{4}$$

For completeness, we introduce a similar decomposition for a scalar field Ψ as

$$\Psi = \sum_{n=1}^{N} \sum_{m=-M}^{M} \sum_{k=-P\pi/2L}^{P\pi/2L} Q^{nmk} J_m(\mu_{nmk}r) \exp(\mathrm{i}m\varphi + \mathrm{i}kz), \tag{5}$$

so that we have

$$\mathrm{GT}(\Psi) = Q^{nmk}. \tag{6}$$

2.4.2. Useful formulae. Our decomposition allows for an interesting representation of usual derivatives, which are a generalization of similar operations in the Fourier space. Indeed, we have for a scalar field

$$\mathrm{GT}(\Delta\Psi) = -(\mu_{nmk}^2 + k^2)Q^{nmk},$$

$$\mathrm{GT}(\nabla\Psi) = \begin{pmatrix} -\dfrac{1}{2}\mu_{nmk}Q^{nmk} \\ \dfrac{1}{2}\mu_{nmk}Q^{nmk} \\ \mathrm{i}kQ^{nmk} \end{pmatrix}. \tag{7}$$

In a similar way, we have for a vector field

$$\mathrm{GT}(\nabla \cdot \mathbf{B}) = \mu_{nmk}\left(C_+^{nmk} - C_-^{nmk}\right) + \mathrm{i}kC_z^{nmk},$$

$$\mathrm{GT}(\nabla \times \mathbf{B}) = \begin{pmatrix} \dfrac{\mathrm{i}}{2}\mu_{nmk}C_z^{nmk} - kC_+^{nmk} \\ \dfrac{\mathrm{i}}{2}\mu_{nmk}C_z^{nmk} + kC_-^{nmk} \\ -\mathrm{i}\mu_{nmk}\left(C_+^{nmk} + C_-^{nmk}\right) \end{pmatrix}. \tag{8}$$

These simple formulae show that once the field has been reconstructed, it is easy to perform accurate derivative operations by working in the Galerkin space. Moreover, the formulae can be used to select a useful special Galerkin basis for magnetic field reconstructions.

2.4.3. Useful basis. A general Galerkin transform of an arbitrary vector field requires three independent coefficients for each (nmk). In the case of a solenoidal field, we must have $\mu_{nmk}(C_+^{nmk} - C_-^{nmk}) + \mathrm{i}kC_z^{nmk} = 0$ for any (nmk), so that only two independent coefficients remain. In the following, we describe even simpler cases, with only one independent coefficient, that are appropriate for fields and boundary conditions usually met in our von Karman experiment.

2.4.4. The Beltrami case. In this case, the Galerkin transform reads

$$\mathrm{GT}(\mathbf{B}) = D_{nmk}\begin{pmatrix} \dfrac{1}{2}\left(\lambda_\pm - k\right) \\ \dfrac{1}{2}\left(\lambda_\pm + k\right) \\ -\mathrm{i}\mu_{nmk} \end{pmatrix}, \tag{9}$$

where the D_{nmk} are complex numbers such that $D_{nmk} = D_{n-m-k}^*$ and $\lambda_\pm = \pm\sqrt{\mu_{nmk}^2 + k^2}$. This corresponds to a decomposition into Beltrami waves, with polarization given by the sign of λ. To guarantee some interesting orthogonality conditions, we further take μ_{nmk} as the nth root of J_m. The corresponding field is solenoidal, and such that $B_z = 0$ at $r = 1$.

2.5. The Marié–Normand–Daviaud field case

There are two cases depending on the axial wave number.

Case $k \neq 0$.

$$\mathrm{GT}(\mathbf{B}) = D_{nmk} \begin{pmatrix} c_+ K_{m+1}/J_{m+1}(\mu_{nmk}) \\ c_- K_{m-1}/J_{m-1}(\mu_{nmk}) \\ K_m/J_m(\mu_{nmk}) \end{pmatrix}, \tag{10}$$

where the D_{nmk} are complex numbers such that $D_{nmk} = D^*_{j-m-k}$, K_m expressed through the modified Bessel function of order m as $K_m = K_m(|k|)$, $c_\pm = \mathrm{i}|k|/k\sqrt{2}$, and the parameter μ_{nmk} is determined as the nth root of the equation,

$$\frac{2|k|}{\mu} \frac{K_m(|k|)}{J_m(\mu)} = \frac{K_{m-1}(|k|)}{J_{m-1}(\mu)} - \frac{K_{m+1}(|k|)}{J_{m+1}(\mu)}. \tag{11}$$

For each k, there is an infinite set of real positive values μ_{nmk}, which we truncate to N, the number of radial modes in the Galerkin expansions (3). Marié *et al* [3] determined the roots of (11) for $m = 1$ and discrete values of the axial wave number ($k\pi/2L$). The roots of (11) for higher values of m, up to $m \leqslant 5$, were computed later by Leprovost [7]. For a given value of k, the successive roots of (11) take increasingly large values as n increases ($\mu_{(n-1)mk} < \mu_{nmk}$). As an example, for $m = 1$ and $k = 1$, their values range between $\mu_{111} = 2.217$ and $\mu_{n11} = 32.22$ for $n = 20$.

Case $k = 0$. In that case, there are two different families of modes.

The first family has the form

$$\mathrm{GT}(\mathbf{B}) = D_{nm0} \begin{pmatrix} \dfrac{1}{2m}\mu_{nm0}/J_{m+1}(\mu_{nm0}) \\[2mm] \dfrac{1}{2m}\mu_{nm0}/J_{m-1}(\mu_{nm0}) \\[2mm] 0 \end{pmatrix}, \tag{12}$$

where μ_{nm0} is the nth root of J_{m-1}.

The second family has the form

$$\mathrm{GT}(\mathbf{B}) = D_{nm0} \begin{pmatrix} 0 \\ 0 \\ 1/J_m(\bar{\mu}_{nm0}) \end{pmatrix} \tag{13}$$

associated with a different set of eigenvalues $\bar{\mu}_{nm0}$ that are the zeros of J_m.

This Galerkin basis is solenoidal and matches at $r = 1$ with a field such that $\Delta \mathbf{B} = \mathbf{0}$. This case is therefore suitable for describing a medium surrounded by an insulating fluid.

2.6. The Ferro case

For this case, we choose

$$\mathrm{GT}(\mathbf{B}) = D_{nmk} \begin{pmatrix} -\mu_{nmk}(k-\gamma) \\ \mu_{nmk}(k-\gamma) \\ \mu_{nmk}^2 \end{pmatrix}, \tag{14}$$

where the D_{nmk} are complex numbers such that $D_{nmk} = D^*_{n-m-k}$, with μ_{nmk} being the nth root of J_m, and γ is the solution of the dispersion equation,

$$\gamma = k \frac{J_{m+1}(\mu_{nmk}) + J_{m-1}(\mu_{nmk})}{J_{m+1}(\mu_{nmk}) - J_{m-1}(\mu_{nmk})}. \tag{15}$$

In this case, the field is solenoidal, and $B_z = B_\phi = 0$ at $r = 1$, i.e. is perpendicular at the boundary at $r = 1$. This case therefore describes the case where the fluid is enclosed inside a ferromagnetic boundary.

2.7. The inverse problem

In the three cases we considered above, the final Galerkin expansion for the magnetic field at a given resolution (N, M, P) requires $2N(M + 1)(2P + 2)$ independent real coefficients[2]. To compute these coefficients, one writes the condition that the Galerkin expansion of **B** matches the measured field $\mathbf{B}_{\mathrm{mes}}$, at different probe locations $(r_{\mathrm{mes}}, \varphi_{\mathrm{mes}}, z_{\mathrm{mes}})$,

$$\mathbf{B}(r_{\mathrm{mes}}, \varphi_{\mathrm{mes}}, z_{\mathrm{mes}}) = \mathbf{B}_{\mathrm{mes}}. \tag{16}$$

This procedure can be recast formally into the equation

$$\mathcal{A}_{ij} X_j = Y_i, \tag{17}$$

where $X_j, j = 1, \ldots, 2N(M + 1)(2P + 2)$ is the vector formed with the real part and the imaginary part of the unknown complex coefficients D_{imk}; $Y_i, i = 1, \ldots, 3N_{\mathrm{mes}}$ is the vector formed by each of the components of the measured magnetic field at each probe location; and $\mathcal{A}_{ij}$ is the matrix formed by the Galerkin basis evaluated at the probe locations. Inverting formally (17), one then obtains the unknown coefficient of the Galerkin expansion through

$$X_i = \mathcal{A}^{-1}_{ij} Y_j, \tag{18}$$

where $\mathcal{A}^{-1}_{ij}$ is the pseudo-inverse of $\mathcal{A}_{ij}$. Indeed, to ensure robustness of the procedure, we choose in the following the resolution such that $2N(M + 1)(2P + 2) \leqslant 3N_{\mathrm{mes}}$ (see the discussion above). The problem is therefore overdetermined so that only the pseudo-inverse is defined (in the sense that there is an infinite number of solutions for (18)). We have tested two Matlab procedures for the pseudo-inverse, resulting in two sets of solutions that are both solutions in the least square sense (i.e. minimizing the norm of $\mathcal{A}_{ij} X_i - Y_j$): one minimizing the norm of X_i (pinverse function) and one minimizing the number of non-zero components of X_i (/function). In addition, we have implemented a standard regularization procedure based on the Tikhonov method using Matlab codes developed by Professor Per Christian Hansen [5] and provided in http://www2.imm.dtu.dk/pch/Regutools/. All three procedures give similar results for smooth fields (for example, time-averaged fields). The regularization method allows the elimination of spurious noise in the case of rough fields (such as instantaneous fields). We have therefore privileged this method in the following. To test the method and its sensitivity to the different parameters, we use two types of fields: (i) synthetic fields, constructed from the Galerkin basis; (ii) real fields, issued from stereoscopic particle image velocimetry (SPIV) performed on a turbulent von Karman water flow, in a half-scale cylindrical vessel with respect to the VKS experiment [17].

---

[2] The factor 2 comes from the complex nature of the coefficients; the factor $(M + 1)$ takes into account the reality of the field, thereby imposing symmetry conditions on the D_{nmk}; and the factor $2P + 2$ takes into account the existence of two families of modes at $k = 0$.
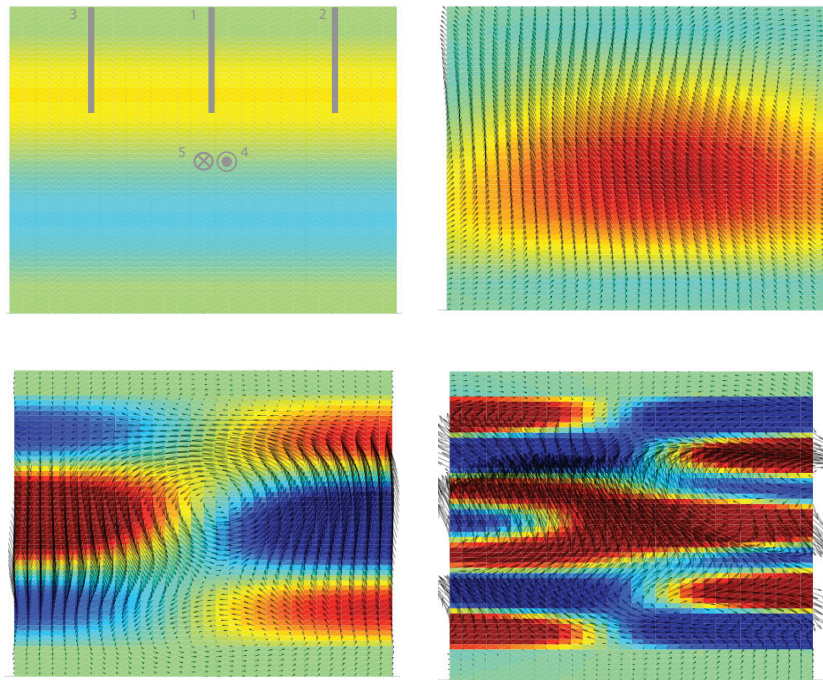
Figure 2. Projection of synthetic fields at different resolutions (N, M, P) in a meridional plane passing through the symmetry axis. The out of plane (toroidal) component B_ϕ is coded with color and the in-plane (poloidal) component (B_r and B_z) are coded with arrows (this representation is used in the whole paper). Top left: $N = 1$, $M = 0$, $P = 0$; top right: $N = 1$, $M = 1$, $P = 1$; bottom left: $N = 2$, $M = 1$, $P = 1$; bottom right: $N = 3$, $M = 2$, $P = 1$. We represent five possible probe locations in the top left figure.

3. Tests on synthetic fields

3.1. Description of synthetic fields

The synthetic fields are constructed from equation (3) by fixing a resolution (N, M, P) and then choosing the $2N(M+1)(2P+2)$-independent D_{nmk} so that the energy is concentrated in the lowest modes and decreases with increasing mode number—the idea being to mimic a 'realistic' experimental field. In practice, we set $D_{nmk} = (-1)^i / i$, where $i = |j| + |m| + |k|$. An example of such synthetic fields is provided in figure 2, for different resolutions (N, M, P).

The complexity of the synthetic field topology increases with the resolution. The synthetic measurements are extracted from these fields by computing the value of the field at some selected location. In the following, we test various reconstructions by using 'measurements' made at the location given by VKS magnetic probes. There are three probes in the vertical plane (probes 1, 2 and 3) and three again in the central plane (probes 1, 4 and 5), at the location of the velocity mixing layer in the exact contra-rotation regime. The location of these probes is reported in figure 2 for illustration and clarity.

3.2. Diagnostic

To quantify the quality of the reconstruction, we define scalar quantities inspired by the classical residue definition as follows. We first divide our available measures into two distinct parts: (i) a large set ($X = \{r_{\text{meas}}^j\}$), including about 95% of the measures, that is kept to reconstruct the field; and (ii) a second, smaller set ($Y = \{r_{\text{test}}^j\}$) that is used to compute 'residue-tests'.

From the first set X, we define a classical residue characterizing the quality of the reconstruction from the measures in the set X as

$$r = \sqrt{\sum_j^N \sum_i^3 \frac{(B_{\text{real}}^i(r_{\text{meas}}^j) - B_{\text{reconst}}^i(r_{\text{meas}}^j))^2}{(B_{\text{real}}^i(r_{\text{meas}}^j))^2}}, \tag{19}$$

with $i = r$, ϕ, z coordinates and $j = 1$, N the number of the measures in X. This residue quantifies the ability of the reconstruction to fit the observed magnetic field with the set of measures X.

From the second set Y, we define another residue based on the measures not involved in the magnetic field reconstruction. This residue is named the *Residue test* and is defined as in equation (19) by substituting r_{meas}^j with r_{test}^j.

Finally, we can define a third residue based on energy as $\Delta E = (E_{\text{synth}} - E_{\text{reconst}})/E_{\text{synth}}$. We refer to it as the energy residue.

3.3. Influence of mode numbers

We first explore the influence of the mode number on the reconstruction. Clearly, we cannot get more reliable information than present in the field to be reconstructed. Therefore, the number of modes used in the reconstruction N_r cannot be larger than the total number of measures $3N_{\text{mes}}$. Also, in order to get stable results, it is interesting to use some redundancy, so that $N_r = (1 - f_r)3N_{\text{mes}}$ where $0 < f_r < 1$ quantifies the percentage of redundancy of the data.

In order to get a hint of typical admissible values of f_r, we use a given (N, M, P) synthetic field with varying $N_r = 2N(M+1)(2P+2)$ modes and extract $3N_{\text{mes}} = 120$ synthetic measures at the VKS sensor positions (ten sensors measuring three components per probe on the 2—3—4—5 probes represented in figure 2). As a preliminary test to check our software, we then first reconstruct the field from the synthetic measure with the same set (N, M, P) of modes. In all cases, we found that the residues are very low ($r \sim 10^{-15}$), i.e. the reconstruction with the same set of modes as the initial field always reproduces well the field at the measurement points. The energy residue is fairly low until $N_r \sim 50$ ($f_r = 0.6$), where the reconstructed energy starts to diverge from the synthetic field energy. Therefore, the degree of redundancy necessary to reconstruct the field in this case must be at least 60%. Respecting these redundancy limitations, we always obtain a quasi perfect reconstruction, giving us good confidence in our software.

The previous situation is, however, quite ideal. In real experiments, the magnetic field has a, presumably fairly large, unknown number of modes, and robust reconstruction attempts use a smaller number of modes than in the experimental field. To test this effect, we choose a synthetic field with a fairly large number of modes ((4, 2, 2) resulting in $N_r = 144$ modes) and reconstruct it with different sets of modes, with $N_r < 96$.

The results are presented in figure 3. We see that the residue decreases fairly monotonically with the energy residue until $N_r \approx 20$($f_r = 0.8$). Above this, the energy residue starts diverging, while the residue continues to decrease until $N_r = 40$ ($f_r = 0.67$), where it saturates towards
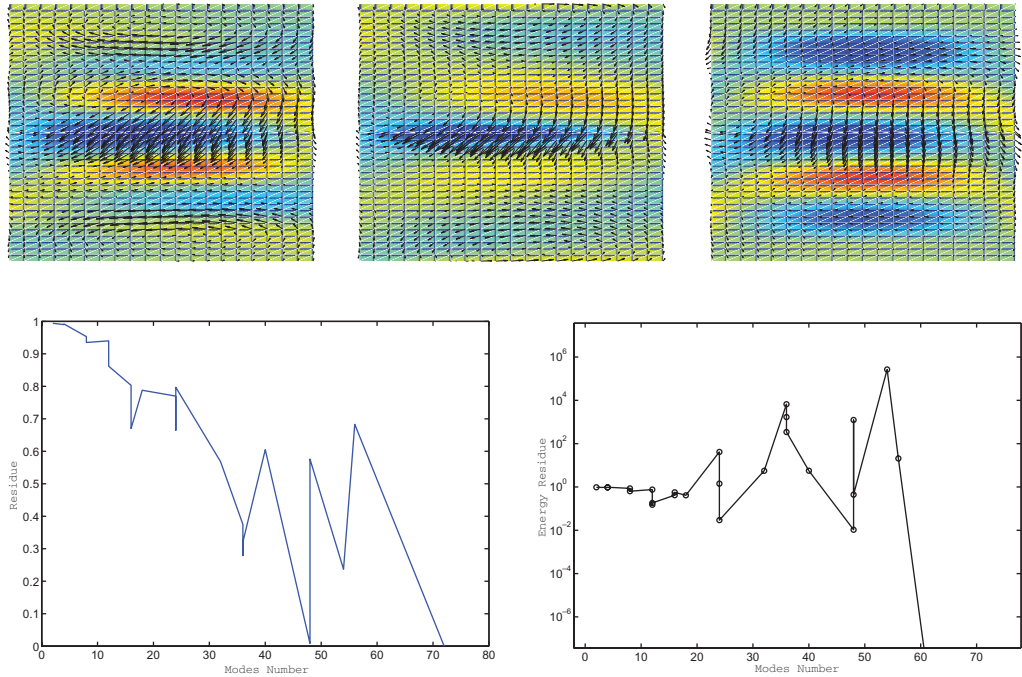
Figure 3. Evolution of the residue (bottom left) and of the energy residue (bottom right) with the magnetic field mode number. The $(4, 2, 2)$ initial field with 144 modes is in the top left figure, the filtered version is represented in the top middle figure and the reconstruction $(3, 1, 1)$ with 48 modes is plotted in the top right figure.

a value of the order of 0.5 (with big oscillations). Note that the oscillations are mainly due to reconstructions that have either $M = 2$ or $P = 2$. These modes are difficult to capture in our measurement setup, because we have a maximum of three values in both the ϕ- and z-directions (see figure 2). Thus, introducing a number of modes superior to one in these directions can lead to systematic error, coming from the low number of measurement points along the z- and ϕ-coordinates. Keeping in mind this restriction, and focusing on reconstruction with $M \leqslant 1$, $P \leqslant 1$, we get a 'best' reconstruction with $(3, 1, 1)$ mode configuration, corresponding to $N_r = 48$ and $\delta E \sim 0.03$ shown in figure 3. One sees that the reconstruction captures the 'large-scale' structure of the initial field. To quantify this further, we may also compare the reconstruction with a filtered version of the initial field, computed using a sgolay filter with a length scale of the order of a tenth of the cylinder radius. One sees that the reconstruction captures even finer details than the coarse version.

3.4. Influence of sensor numbers

In this section, we explore the dependence of the reconstruction quality with the number of sensors (varying N_{mes} the number of measurement points). For this, we consider a $(2, 1, 1)$ synthetic field and reconstruct it with a varying number of measurements $3N_{mes}$. In order to minimize the influence of probe location, we always consider the same number of sensors $N_s/4$ on each of the four probes (probes 2, 3, 4 and 5 reported in figure 2). The number of
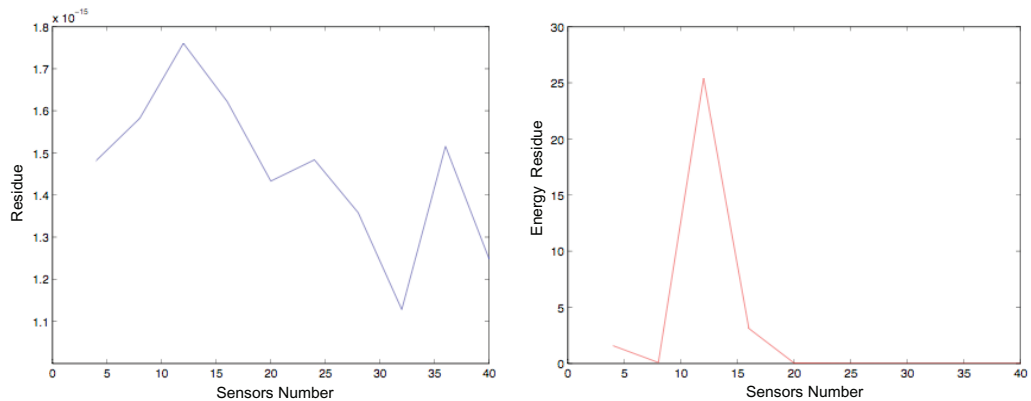
Figure 4. Evolution of the residue (right panel) and energy residue (left panel) of the reconstruction with varying sensor number N_s. There are $N_s/4$ measurements per probe. Here, both the initial and the reconstructed field have 32 modes.

measurements is then increased with increasing N_s. The total number of measurements is then $3N_{mes} = 3N_s$. In the following, we vary $N_s/4$ from 1 to 4. The synthetic fields are reconstructed with a $(2, 1, 1)$ set of modes, with $N_r = 32$.

The influence of N_s on the reconstruction is given in figure 4. The residue is almost constant, maintaining very low values ($r \sim 10^{-15}$). The energy residue ΔE is more sensitive to N_s and takes very large values for $N_s \leqslant 12$, i.e. a total measurement number less than 36. This corresponds precisely to a range of values for which $N_r = 32 > 3(1 - 0.67)N_{mes}$, confirming the importance of keeping at least 60% of redundancy. Above the value $N_s = 12$, the energy residue becomes quite low ($\sim 10^{-5}$) and the reconstruction quality is excellent.

3.5. Influence of probe location

We have worked so far assuming that the measurements are carried out at the present VKS probe location (see figure 2). It is, however, interesting to check the influence of the probe location on the reconstruction, so as to potentially optimize experimental measurements. The question is then how to optimize the probe location to get the maximal quality of magnetic field reconstruction with minimal impact on the experimental sodium flow. Such an impact is decreased with a decreasing number of probes and with a probe configuration respecting as much as possible the symmetries of the flow. We thus consider now measurements carried out with only two probes. Given the present experimental configuration, three different sets of symmetric probe locations can then be constructed. They are reported in figure 5.

The three configurations are (i) the *axial configuration* with two probes in the same vertical plane symmetric with respect to the meridional plane; (ii) the *central configuration* with two probes in the meridional plane of the cylinder ($z = 0$) at two angles differing by π; and (iii) the *shifted configuration* with two probes at different z and different ϕ angles. We consider ten sensors on each probe, and reconstruct the fields with the same increasing number of modes for both the synthetic field and the reconstructed field.

The residue behavior for the three configurations is given in figure 5. The residue in the central configuration is large and decreases with the mode number, while it is small or close to zero for axial and shifted configurations. The energy residue for the axial and central
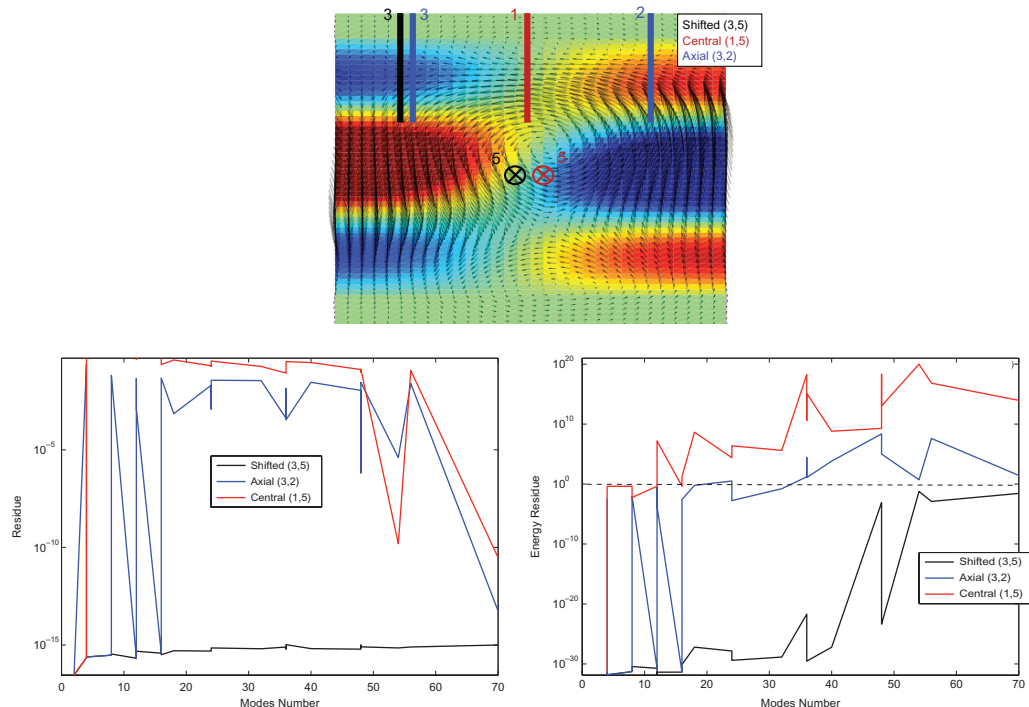
Figure 5. Top figure: an example of a synthetic field with the indication of the three-probe configuration (axial, central, shifted). Bottom: evolution of residue (left) and energy residue (right) with number of initial field modes (equal to the number of reconstructed modes) depending on the three sets of probes' location axial, central and shifted.

configuration increases significantly with the mode number. Thus, the reconstruction in this geometry is not reliable with only two probes. In contrast, the shifted configuration provides fairly reasonable results. We focus on this configuration from now on.

3.6. Influence of noise

So far, we have performed reconstruction using 'perfect' measures, matching exactly the synthetic field. In real experiments, various noise sources pollute the measurements, and it is important to test the sensitivity of the reconstruction to measurement noise. We therefore extract artificial measurements from a synthetic $(4, 2, 2)$ field (144 modes) in a *shifted configuration* and superimpose on them a white noise of increasing amplitude $A_{noise} = R_{noise}/R_{meas}$ before reconstructing the field. We consider two cases: (i) a reconstruction with the same number of modes as the synthetic field and varying noise amplitude. The results are provided on the left panel of figure 6. (ii) A reconstruction using an under-sampled number of modes ($N_r = 48$ for $(3, 1, 1)$)—to remain close to actual experimental conditions—and varying noise amplitude. The results are provided on the right panel of figure 6.

In all cases, we observe a decrease in the reconstruction quality with increasing noise. The impact is larger for the under-sampled case but grows less rapidly. The energy residue, however, stays close to the initial energy. Our conclusion is that the energy measurements from reconstruction techniques are reliable up to 20% even in the presence of noise.
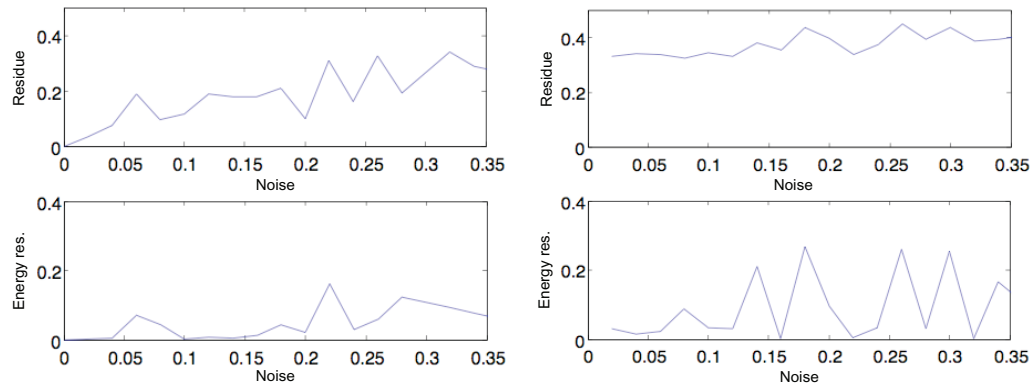
Figure 6. Evolution of the residue and energy residue with the noise intensity. On the left panel, the reconstructed and the initial field have the same set of modes; on the right panel, the reconstructed field has a lower number of modes than the initial field.

From our series of tests, we obtained two main conditions for reliable reconstruction: shifted probe configuration and the number of reconstruction modes smaller than the number of measurements. Furthermore, we observed that the residue by itself is not a reliable test of the reconstruction quality, since we can get very good residue and poor energy residue. Since, in experimental fields, we dot not have access to the energy of the field (i.e. we cannot compute energy residue), we shall use the residue test to discriminate the reconstruction quality.

4. Test on a real field

Until this point, we have focused on tests of our inversion procedure using synthetic field and artificial noise. Before implementing our procedure in actual data, we first tried to see if it is experimentally sound, i.e. whether it is able to reconstruct a real and known soleinodal field, from experimental measurements. We did not have at our disposal a known experimental magnetic field. However, we had in store an experimental velocity field measured through an SPIV on a Von Karman water flow. This provides an experimental picture of the three components of a soleinodal field in a meridional plane passing through the axis of rotation, which can be used to further test our reconstruction method. Indeed, we can introduce three 'fictive probes' in our device (see figure 7) and use them to extract 30 artificial measurements. Using our inversion procedure, we can then reconstruct the field from these measurements, and compare the result with the actual measurement to check the soundness of the result. This has been done with an experimental velocity field measured in counter-rotation at a frequency of 16 Hz [23]. The time-averaged velocity field is shown in figure 7. It is obviously a fairly large-scale axisymmetric field, with four recirculating cells. To test the reconstruction, we extract 30 artificial measurements from three fictive probes located at the locations of the VKS experiment, shown in figure 7. We then reconstruct this field using the inversion procedure described in section 2, using the Galerkin basis based on Beltrami waves (see section 2.4.4).

Since the flow is axisymmetric, we consider only cases with $M = 0$. The result of the reconstruction is provided in figure 7, for $(5, 0, 1)$ modes. The associated residue is 0.26, while the energy residue is 0.25. Comparing with the full experimental field, we see that the
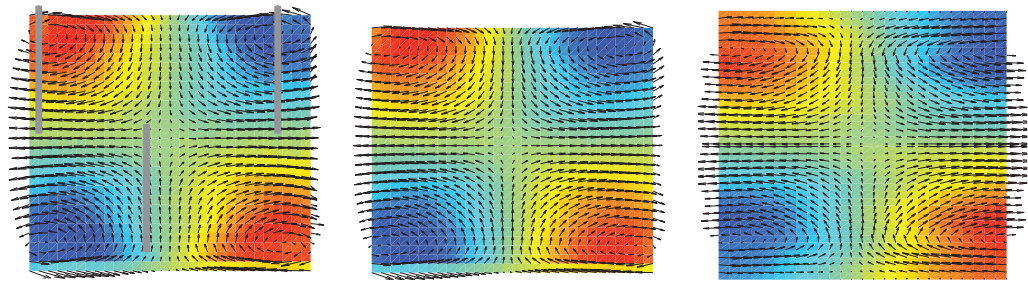
Figure 7. On the left panel, a real Von Karman water velocity field ($F = 16$ Hz); on the middle panel, the filtered version; and on the right panel, the reconstructed field. The out of plan (toroidal) component V_ϕ is coded with color (red is positive values while blue is negative values) and the in-plane (poloidal) component (V_r, V_z) is coded with arrows. The three probes of ten sensors used to reconstruct the field are represented in gray on the left panel.

main topology of the velocity field is well captured: the cell limits are close to reality and their amplitudes near the center are well reproduced. However, the positions of the maxima of each cell are not well reproduced and the velocity amplitude of in-plane components is overestimated near the discs. To check whether this is an effect of 'under-resolution', we also made a comparison with a filtered version of the experimental field, using a sgolay filter, so as to keep only the largest scale. One sees that indeed the position of the maxima of each cell is closer to that of the filtered field.

Note that we reconstructed this topology from an axial configuration of probes (the only one available in this situation), which is not as reliable as a shifted configuration, as proved in section 3.5.

From this test over an experimental field, we conclude that the reconstruction is able to extract general behavior (energy and global topology) of a given field from a restrained number of measures. Smaller-scale details, such as the exact maxima positions, or the field amplitudes near the boundaries, require a much larger number of measurements, which are for the moment unavailable in the VKS experiment.

5. Application to the von Karman sodium (VKS) experiment

In this section, we finally apply the reconstruction method to the magnetic field in a particular VKS experiment. We consider a setup with two iron impellers. The flow is surrounded by sodium at rest in an outer cylinder (radius $R_c = 289$ mm, length 604 mm) delineated by a copper cylinder. This configuration is discussed at length in [20]. In exact counter-rotation, it leads to a statistically stationary dynamo for $F_1 = F_2 > 16$ Hz. Measurements are made through three probes: one probe with ten sensors, located at position 5 in figure 2 (SM1), one probe with eight sensors, at position 2 (SM2), and a Gaussmeter (one sensor), in position 3 (G). Due to failure of some experimental probes, we can consider only a restricted number of reliable measures for reconstruction. Here, we focus on seven exact contra-rotation regimes at frequencies ($F_1 = F_2 = 12, 17, 18, 19, 20, 21, 22$ Hz) corresponding to a magnetic Reynolds number $Rm = 0.6 \, \mu_0 \sigma (F_1 + F_2)/2\pi R_C^2$ at temperature 120 °C $Rm = 24, 34, 36, 38, 40, 42$ and 44. The last six regimes in this study correspond to the dynamo regime. For each regime,
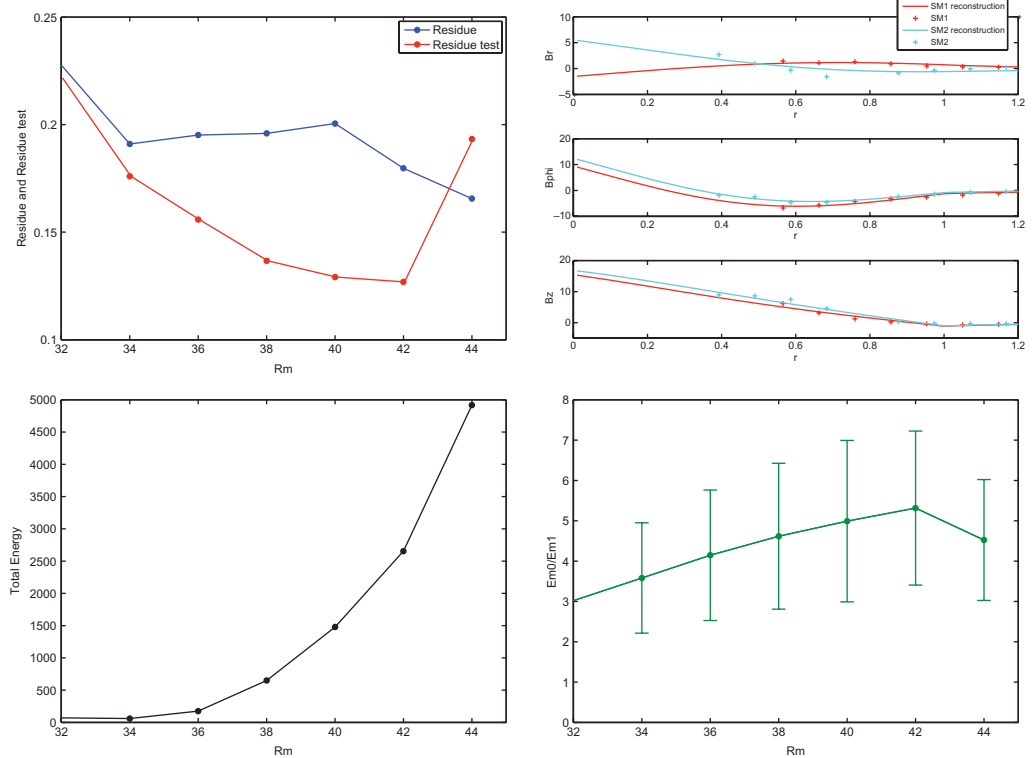
Figure 8. Top left: reconstruction residue (in blue) and residue test (in red) for different magnetic Reynolds number in a VKS2 experiment. Top right: comparison between reconstructed field (lines) and real probe measures (crosses); one sees that the reconstruction captures the behavior well. Bottom left: total energy of the reconstruction as a function of magnetic Reynolds number. Bottom right: ratio of the energy of $m = 0$ modes on the energy of $m = 1$ modes as a function of the magnetic Reynolds number. We also add the error bars extracted from the residue.

measurements are made during 60 s at a frequency of 2000 Hz. In order to extract a general large-scale behavior, we average in time the measurements at each frequency. According to the results of the previous section, our measurement number prevents reconstruction of the magnetic field with more than 54 modes.

We then reconstruct the field with a non-axisymmetric set of modes: $(2, 1, 1)$ corresponding to 32 modes (the maximum number of modes we can reconstruct the magnetic field with). We compute the residue and the residue test taken on one of the sensors of SM1 (as defined in section 3.2). These residues for different Rm are shown in figure 8. The $(2, 1, 1)$ set of modes gives a residue ~ 0.2 and a residue test ~ 0.15 for the dynamo regimes. This set of modes provides a reasonable fit of the measurement, as seen in figure 8. Its corresponding total energy as a function of Rm is given in figure 8. The total energy growth is roughly quadratic in Rm.

A first striking result of our reconstruction is that the time averaged dynamo field is not purely axisymmetric: $m = 1$ mode is needed to fit the measurements. To quantify this result, we show in figure 8 the ratio of the energy of the $m = 0$ mode to the energy of the $m = 1$ mode.
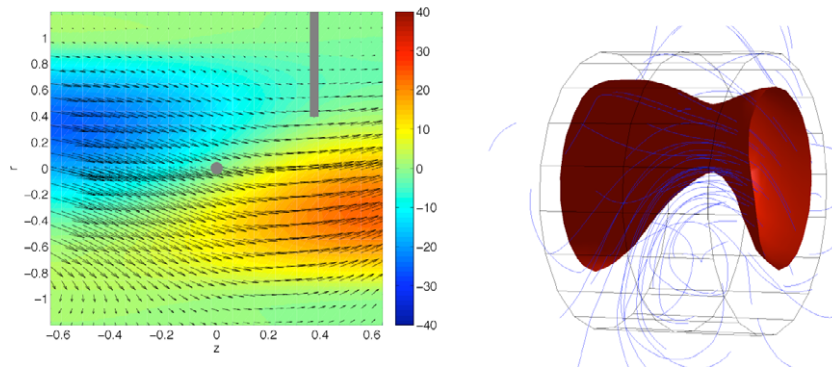
Figure 9. Left: total reconstructed magnetic field in a VKS experiment at $Rm = 34$, just above dynamo onset. The out-of-plane (toroidal) component B_ϕ is coded with color and the in-plane (poloidal) component (B_r, B_z) is coded with arrows. Right: corresponding stream lines and energy density at 25% of the maximum.
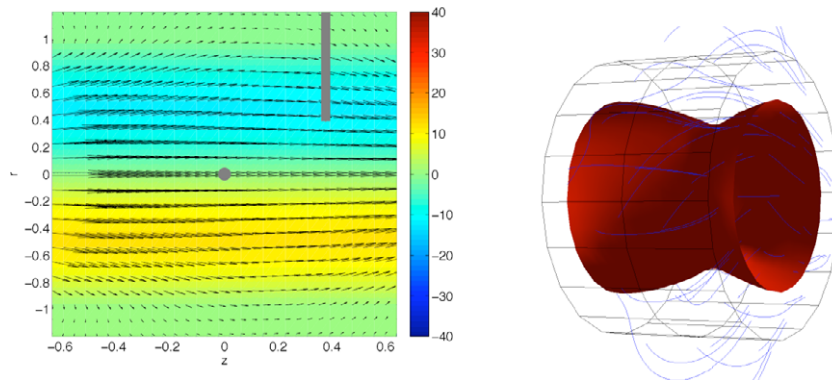

Figure 10. Left: mode $m = 0$ of the reconstructed magnetic field in a VKS experiment at $Rm = 34$, just above the dynamo onset. The out-of-plane (toroidal) component B_ϕ is coded with color and the in-plane (poloidal) component (B_r, B_z) is coded with arrows. Right: corresponding stream lines and energy density at 25% of the maximum.

We see that this ratio increases with Rm: the dynamo becomes more and more axisymmetric. However, the mode $m = 1$ does not disappear and still contains a significant amount of energy at the largest Rm: for $Rm = 34$, $E_{m=0}/E_{m=1} = 1.8$; for $Rm = 44$, $E_{m=0}/E_{m=1} = 5.4$.

The corresponding dynamo field structure is given in figure 9 at $Rm = 34$ close to the dynamo onset. It is mainly an axial dipole, with a concentration of azimuthal energy near the iron propellers. Taking a closer look at this phenomenon through iso-density of energy surface at 25% of the maximum energy (figure 9), we observe that the energy distribution is asymmetric, with more energy close to the left disc than close to the right disc. At present, we do not know whether this is an artifact of the reconstruction due to the lack of measurements or if this reflects an actual breaking of the axial symmetry across the $z = 0$ plane, generated by the dynamo. More measurements are needed.

To try and determine the nature of the two modes, we plot them separately in figure 10 for the $m = 0$ mode and in figure 11 for the $m = 1$ mode. The $m = 0$ mode is clearly an axial dipole,
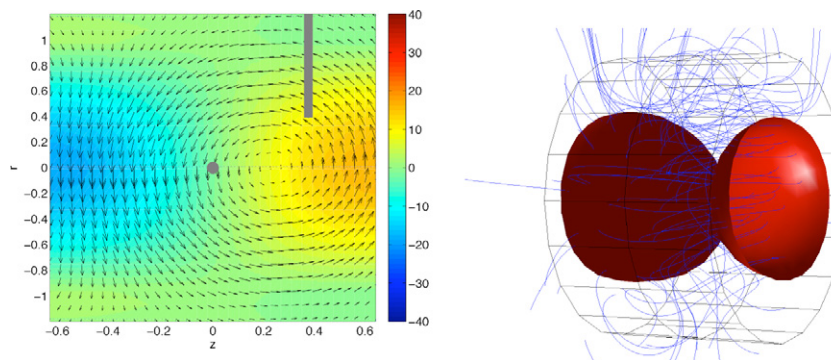
Figure 11. Left: mode $m = 1$ of the reconstructed magnetic field in a VKS experiment at $Rm = 34$, just above the dynamo onset. The out-of-plan (toroidal) component B_ϕ is coded with color and the in-plane (poloidal) component (B_r, B_z) is coded with arrows. Right: corresponding stream lines and energy density at 25% of the maximum.

as already discussed in [13]. The $m = 1$ mode has a meridional dipole component, localized near the propeller which concentrates the largest energy. It does not, however, resemble the neutral mode predicted by kinematic dynamos based on the mean velocity flow [3]. This result is interesting, because it may provide some hints about the origin of the $m = 0$ and $m = 1$ modes in our reconstruction. In the absence of any probes in our device, the mean velocity field is perfectly axisymmetric, and can only support kinematic growth of an $m = 1$ mode. In the presence of non-axisymmetric helical fluctuations, however, an $m = 0$ dynamo mode can grow through a simple $\alpha-\omega$ mechanism [27, 28, 30]. In the presence of a soft iron impeller, the growth of the $m = 0$ mode is favored against the $m = 1$ mode [29]. In the present case, we have an additional source of non-axisymmetry, via either the earth magnetic field or the presence of the probes that break the axisymmetry of the flow. Our observation that the $m = 1$ mode does not resemble the kinematic $m = 1$ mode suggests that it is a perturbation linked with external non-axisymmetry of the experiment (through either probes or the earth field). This means that we may be in an intermediate Reynolds number regime, where the $m = 0$ dynamo mode is permitted but not the $m = 1$ kinematic mode.

To quantify further how the repartition between the $m = 0$ and $m = 1$ modes proceeds during dynamo instability, we apply a reconstruction procedure during the growth of the magnetic field. For this, we consider dynamical measurements at $Rm = 32$, during a growth stage, and apply a moving average over 0.1 s upon all measurements. We then reconstruct in time the magnetic field in order to get the mode topology during the growth. The result is given in figure 12, where the normalized magnetic energy measured in the experiment is compared with the relative energy ratios $E_{m=0}/(E_{m=0} + E_{m=1})$ and $E_{m=1}/(E_{m=0} + E_{m=1})$ obtained through the reconstruction. In this measurement, the experiment is tuned at a value of Rm larger than critical at $t = 0$. The magnetic field then increases in time due to the dynamo instability. One sees that at the very early stage of the growth, the mode $m = 1$ dominates, with an occasional crossover with the mode $m = 0$ corresponding to a localized magnetic energy burst. Then, after about 30 s, the magnetic field growth accelerates, corresponding to a crossover between the $m = 1$ and $m = 0$ modes, which predominates after this stage. Note further that the magnetic field growth proceeds in roughly three steps: one between $t = 0$ and $t = 30$ where the magnetic
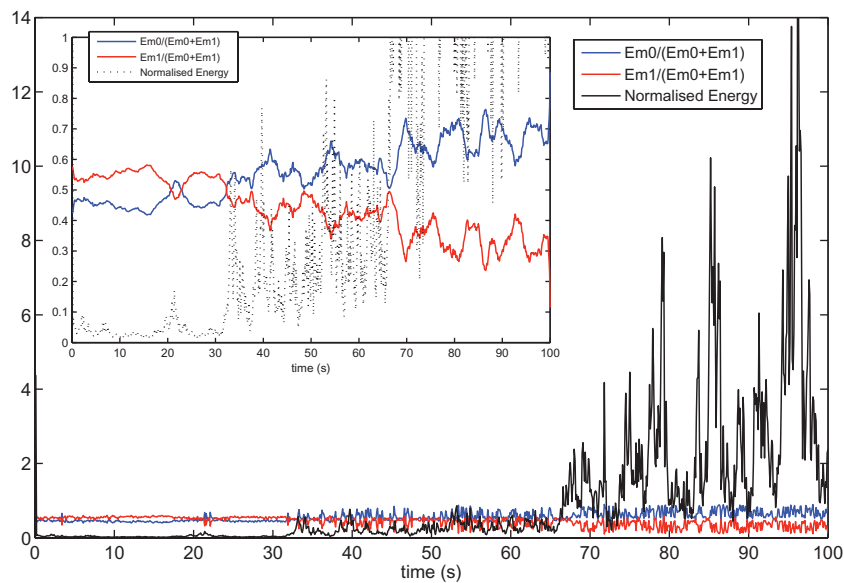
Figure 12. Total energy, $m = 0$ and $m = 1$ mode relative energies as a function of time during the initial growth of the magnetic field ($Rm = 36$). Inset: zoom of the evolution at early time, to capture the crossover behavior.

field is small, with only one energy burst (corresponding to the first crossover in between the $m = 0$ and $m = 1$ modes); a second stage, corresponding to the crossover between the $m = 0$ and $m = 1$ modes, with larger fluctuations, but still moderate values of the magnetic field; and a third stage, from $t = 60$, where the energy explodes and the dynamo settles, with a predominance of the $m = 0$ mode.

This interesting step-by-step dynamo onset suggests that the dynamo mechanism is non-trivial, and may involve the action of the $m = 1$ as a catalyst. Further analysis with more measurements will be necessary in order to clarify this point.

6. Discussion

We have presented a method of reconstruction for 3D magnetic field reconstruction based on Galerkin transforms and tested it over synthetic fields and real solenoidal (velocity) fields, measured in a water experiment. Our study shows that reliable reconstructions are possible provided that the probes are sufficiently sampled and located in shifted configurations. The present sets of available measurements in VKS experiments prevent reconstruction of modes higher than $m = 1$. In that respect, it would be interesting to develop azimuthal belt probes around the cylinder in order to extract $m > 1$ modes without perturbing the flow with intrusive sensors. To illustrate the possibility of our method, we have applied it to an old VKS experimental configuration. Due to the fairly low available number of measurements, we could only obtain rough results regarding the dynamo geometry, confirming previous results. In future VKS dynamo campaigns, as many as four probes with ten sensors each will be available. We therefore hope that reconstruction in such a case will be more reliable, and that we can gain interesting results concerning the magnetic field geometry during dynamical events (reversals, periodic cycles, extinction, bursts, etc. [14]) that can help in improving our understanding of turbulent dynamos.

IOP Institute of Physics ⬧ DEUTSCHE PHYSIKALISCHE GESELLSCHAFT

Acknowledgments

References

[1] Solanki S K, Lagg A, Woch J, Krupp N and Collados M 2003 *Nature* **425** 692
[2] Hu L, Zou J, Fu X, Yang Y H, Ruan X D and Wang C Y 2009 A reconstruction approach to determining the magnetic field around an electromagnetic velocity probe *Meas. Sci. Technol.* **20** 015103
[3] Marié L, Normand C and Daviaud F 2006 Galerkin analysis of kinematic dynamos in the von Kármán geometry *Phys. Fluids* **18** 017102
[4] Normand C 2008 Modal versus energy stability analysis of kinematic dynamos in cylindrical configurations *Phys. Fluids* **20** 084105
[5] Hansen P C 1994 Regularization tools: a Matlab package for analysis and solution of discrete ill-posed problems *Numer. Algorithms* **6** 1–35
[6] Marié L 2003 Transport de moment cinétique et de champ magnétique par un écoulement tourbillonnaire turbulent: influence de la rotation *PhD Thesis* Université Paris 7
[7] Leprovost N 2004 Influence des petites échelles sur la dynamique a grande échelle en turbulence hydro et magnétohydrodynamique *PhD Thesis* Université Paris 6
[8] Bourgoin M 2002 Magnetohydrodynamics measurements in the von Karman sodium experiment *Phys. Fluids* **14** 3046
[9] Shew W L, Sisan D R and Lathrop D P 2002 Mechanically forced and thermally driven flows in liquid sodium *Magnetohydrodynamics* **38** 121
[10] Forest C B, Bayliss R A, Kendrick R D, Nornberg M D, O'Connell R and Spence E J 2002 Hydrodynamic and numerical modeling of a spherical homogeneous dynamo experiment *Magnetohydrodynamics* **38** 107
[11] Gailitis A *et al* 2000 Detection of a flow induced magnetic field eigenmode in the Riga dynamo facility *Phys. Rev. Lett.* **84** 4365
[12] Stieglitz R and Müller U 2001 Experimental demonstration of a homogeneous two-scale dynamo *Phys. Fluids* **13** 561
[13] Monchaux R *et al* 2007 Generation of magnetic field by dynamo action in a turbulent flow of liquid sodium *Phys. Rev. Lett.* **98** 044502
[14] Monchaux R *et al* 2009 The von Kármán sodium experiment: turbulent dynamical dynamos *Phys. Fluids* **21** 035108
[15] Marié L, Burgete J, Daviaud F and Léorat J 2003 Numerical study of homogeneous dynamo based on experimental von Karman type flows *Eur. Phys. J.* B **33** 469
[16] Ravelet F, Chiffaudel A, Daviaud F and Léorat J 2005 Toward an experimental von Karman dynamo: numerical studies for an optimized design *Phys. Fluids* **17** 117104
[17] Ravelet F, Chiffaudel A, Daviaud F and Léorat J 2005 Towards a von Kármán dynamo: numerical studies based on experimental flows *Phys. Fluids* **17** 117104
[18] Pétrélis F, Bourgoin M, Marié L, Burguete J, Chiffaudel A, Daviaud F, Fauve S, Odier P and Pinton J-F 2003 Nonlinear magnetic induction by helical motion in a liquid sodium turbulent flow *Phys. Rev. Lett.* **90** 174501
[19] Marié L, Pétrélis F, Bourgoin M, Burguete J, Chiffaudel A, Daviaud F, Fauve S, Odier P and Pinton J-F 2002 Open questions about homogeneous fluid dynamos: the VKS experiment *Magnetohydrodynamics* **38** 156–69
[20] Berhanu M *et al* 2010 Dynamo regimes and transitions in the VKS experiment *Eur. Phys. J.* B **77** 459

IOP Institute of Physics ⬥ DEUTSCHE PHYSIKALISCHE GESELLSCHAFT

[21] Fauve S and Pétrélis F 2008 Chaotic dynamics of the magnetic field generated by dynamo action in a turbulent flow *J. Phys.: Condens. Matter* **20** 494203

[22] Naso A, Monchaux R, Chavanis P H and Dubrulle B 2010 Statistical mechanics of Beltrami flows in axisymmetric geometry: theory revisited *Phys. Rev.* E **81** 066318

[23] Cortet P-P, Diribarne P, Monchaux R, Chiffaudel A, Daviaud F and Dubrulle B 2009 Normalized kinetic energy as a hydrodynamical global quantity for inhomogeneous anisotropic turbulence *Phys. Fluids* **21** 025104

[24] Iskakov A, Descombes S and Dormy E 2005 On magnetic boundary conditions for non-spectral dynamo simulations *Geophys. Astrophys. Fluid Dyn.* **99** 481

[25] Guermond J-L, Laguerre R, Léorat J and Nore C 2007 An interior penalty Galerkin method for the MHD equations in heterogeneous domains *J. Comput. Phys.* **221** 349

[26] Stefani F, Xu M, Gerbeth G, Ravelet F, Chiffaudel A, Daviaud F and Léorat J 2006 Ambivalent effects of added layers on steady kinematic dynamos in cylindrical geometry: application to the VKS experiment *Eur. J. Mech.* B **25** 894

[27] Laguerre R, Nore C, Ribeiro A, Léorat J, Guermond J-L and Plunian F 2008 Impact of impellers on the axisymmetric magnetic mode in the VKS2 dynamo experiment *Phys. Rev. Lett.* **101** 104501

[28] Pétrélis F, Mordant N and Fauve S 2007 On the magnetic fields generated by experimental dynamos *Geophys. Astrophys. Fluid Dyn.* **101** 289

[29] Giesecke A, Stefani F and Gerbeth G 2010 Role of soft-iron impellers on the mode selection in the von Karman-sodium dynamo experiment *Phys. Rev. Lett.* **104** 044503

[30] Gissinger C 2009 A numerical model of the VKS experiment *Eur. Phys. Lett.* **87** 39002